Decoupled Deblurring Filter and its Application to Elastic Migration and Inversion

Zongcai Feng
King Abdullah University of Science and Technology (KAUST)

ABSTRACT

Parameters of different classes, such as the P- and S-wave velocities, can be coupled to one another in multiparameter seismic inversion. This coupling effect generates crosstalk artifacts in the migration and inversion images. Conventional approximations to the Hessian inverse for a single parameter class usually ignores this coupling effect. We now present a deblurring filter that approximates the multiparameter Hessian inverse. It takes into account the coupling of parameters by using local deblurring filters to approximate the submatrices of the Hessian inverse for different parameter classes. Numerical tests show that the decoupled deblurring filter not only reduces the footprint noise, balances the amplitude and increases the resolution of the elastic migration images, but also mitigates the crosstalk artifacts . When used as a preconditioner, it also accelerates the convergence rate for elastic inversion.

INTRODUCTION

Conventional migration can be considered as the first iteration of iterative least-squares inversion (Claerbout, 1992), where the migration image is obtained by applying the adjoint of the forward modeling operator to the data (Lailly, 1983). The migration operation does not compute the Hessian inverse so the image suffers from amplitude distortion due to uneven illumination, strong footprint noise due to the limited acquisition geometry and blurring effects due to the band-limited wavefields (Nemeth et al., 1999; Aoki and Schuster, 2009). In the multiparemeter case, the Hessian matrix (or its inverse) contains submatrices for different parameter classes that describe the coupling effects (Wang and Pratt, 1997; Operto et al., 2013). Therefore the multiparameter migration image also suffers from crosstalk artifacts. Approaches to partly remedy these imaging problems are based on the seismic inverse theory (Lailly, 1983).

An indirect approach to account for the Hessian inverse relies on iteratively solving either the linear (Lailly, 1984; Nemeth et al., 1999; Duquet et al., 2000) or nonlinear (Tarantola, 1984; Mora, 1987) optimization problem using a gradient-based inverse method, without explicitly calculating the Hessian inverse (Tang, 2009). The quality of the image is iteratively improved. However, the drawback is that the iterative solution can be more than an-order-of-magnitude more costly than standard migration without proper preconditioning (Aoki and Schuster, 2009). In the multiparameter case, the convergence rate and inversion accuracy can be even worse because inversion suffers even more because of the non-linearities (Operto et al., 2013).

The Hessian matrix and its inverse are usually too expensive to compute and store for large-scale 3D applications. The simplest way to reduce the cost is to approximate it by a diagonal matrix (Rickett, 2003; Nemeth et al., 1999; Plessix and Mulder, 2004; Symes, 2008). Recently, Wang et al. (2016) extended the diagonal approximation to the multiparameter case by also estimating the diagonals of the Hessian submatrices for different parameter classes. However, for a finite range of frequencies, the Hessian matrix is diagonally dominant but not diagonal, assuming a dense acquisition geometry. A diagonal approximation to the Hessian matrix can remedy the uneven illumination problem but not the deblurring problem.

The near-diagonal elements of the Hessian matrix are usually approximated (Tang, 2009). Hu et al. (2001) and Yu et al. (2006) estimated the Hessian inverse in the wavenumber domain by assuming a locally layered medium and a sufficiently wide recording aperture. Guitton (2004) approximated the Hessian inverse with a bank of nonstationary matching filters. The matching filter is approximated from the initial image and a second image obtained by migrating the data modelled from the initial image. Similarly, Aoki and Schuster (2009) proposed a bank of local-

ized stationary filters, called the deblurring filters, to approximate the Hessian inverse. Their filters are calculated from a reference model constructed from isolated point diffractors and its migration image. Dai et al. (2011) used the deblurring filter to accelerate the convergence speed of least-squares migration. Recently, the isolated point diffractors are also used to construct models to approximate the multiparameter Hessian (Tang and Lee, 2015).

We now develop a decoupled deblurring filter to estimate the inverse to the elastic multiparameter Hessian matrix, using the localized filter technique similar to Aoki and Schuster (2009). We also construct the multiparameter reference models using isolated point diffractors for different parameter classes. The filters and reference models are designed according to the characteristics of the Hessian inverse. The decoupled deblurring filter estimates the near-diagonal elements of the submatrices of the Hessian inverse for both the same and different parameter classes.

Our decoupled deblurring filter is tested for its effectiveness with the elastic migration and linearized inversion methods applied to elastic data (Duan et al., 2016; Feng and Schuster, 2016). The elastic migration and inversion images contain the reflectivity images of P- and S-wave velocities. The results show that our decoupled deblurring filter not only balances the amplitude, increases the resolution, but also reduces the crosstalk artifacts in the elastic images. It can also be used as a preconditioner to accelerate the convergence of elastic inversion.

This article is organized into four sections. After the introduction, the second section describes the theory of decoupled deblurring filters. Numerical results on the synthetic data are presented in the third section. The synthetic examples are for elastic migration and inversion using the 2D elastic synthetic data. Finally, discussions and conclusions are presented in the last two sections.

THEORY

Linearized forward modeling of seismic data is mathematically represented by the modeling operator $\mathbf{L}$ (Aoki and Schuster, 2009; Dai et al., 2011), so that

$$\mathbf{d} = \mathbf{L}\mathbf{m}, \tag{1}$$

where $\mathbf{d}$ represents the scattered seismic data, $\mathbf{m}$ is the reflectivity model, and $\mathbf{L}$ is the forward modeling operator associated with a specific survey geometry, source wavelet and background velocity parameters. The least-squares inversion of the data for the reflectivity model $\mathbf{m}$ can be represented by

$$\mathbf{m} = (\mathbf{L}^T\mathbf{L})^{-1}\mathbf{L}^T\mathbf{d}, \tag{2}$$

where $\mathbf{L}^T$ is the adjoint of the forward model and $(\mathbf{L}^T\mathbf{L})^{-1}$ is the Hessian inverse. In comparison, migration is the adjoint of the forward modeling operator applied to the data and can be represented by (Claerbout, 1992)

$$\mathbf{m}^{\text{mig}} = \mathbf{L}^T\mathbf{d}, \tag{3}$$

where $\mathbf{m}^{\text{mig}}$ is the migration image. Equation 3 defines the relationship between the migration image and the actual reflectivity model by substituting equation 1 to obtain

$$\mathbf{m}^{\text{mig}} = \mathbf{L}^T\mathbf{L}\mathbf{m}. \tag{4}$$

Equation 4 says that the standard migration image is a blurred version of the actual reflectivity model $\mathbf{m}$ (Hu et al., 2001; Yu et al., 2006), where the blurring operator is $\mathbf{L}^T\mathbf{L}$.

In addition, equation 2 can be written as

$$\mathbf{m} = (\mathbf{L}^T\mathbf{L})^{-1}\mathbf{m}^{\text{mig}}, \tag{5}$$

where the Hessian inverse $(\mathbf{L}^T\mathbf{L})^{-1}$ in equation 5 has many properties. We can improve the quality of the migration image by applying an accurate estimate of $(\mathbf{L}^T\mathbf{L})^{-1}$ to it.

For nonlinear seismic inversion, it is convenient to approximate $\mathbf{d}$ as a truncated Taylor series $\mathbf{d} \approx \mathbf{d}_0 + \frac{\partial \mathbf{d}}{\partial \mathbf{m}}\mathbf{m}$ expanded about the background model $\mathbf{m}_0$ so that

$$\mathbf{L} = \frac{\partial \mathbf{d}(\mathbf{m}_0)}{\partial \mathbf{m}}. \tag{6}$$

Here, $\mathbf{L}$ is called the sensitivity kernel (Virieux and Operto, 2009). Using $(\mathbf{L}^T\mathbf{L})^{-1}$ as the approximate Hessian inverse is referred to as the Gauss-Newton method (Pratt et al., 1988). In this article, the decoupled deblurring filter is mainly illustrated using linearized seismic inverse theory.

Multiparameter Hessian Interpolation

The forward modeling operator $\mathbf{L}$, reflectivity model $\mathbf{m}$ and corresponding migration image $\mathbf{m}^{\text{mig}}$ for p multiparameter classes can be expressed as

$$\mathbf{L} = (\mathbf{L}_1, \mathbf{L}_2, \cdots, \mathbf{L}_p),\ \mathbf{m} = \begin{pmatrix} \mathbf{m}_1 \\ \mathbf{m}_2 \\ \vdots \\ \mathbf{m}_p \end{pmatrix},\ \text{and}\ \mathbf{m}^{\text{mig}} = \begin{pmatrix} \mathbf{m}_1^{\text{mig}} \\ \mathbf{m}_2^{\text{mig}} \\ \vdots \\ \mathbf{m}_p^{\text{mig}} \end{pmatrix}, \tag{7}$$

where $\mathbf{m}_i$ is the model of ith parameter class, $\mathbf{L}_i$ is the linearized forward modeling operator associated with $\mathbf{m}_i$, and $\mathbf{m}_i^{\text{mig}}$ is the migration image of ith parameter class.

The multiparameter Hessian $\mathbf{L}^T\mathbf{L}$ has the form

$$\mathbf{L}^T\mathbf{L} = \begin{pmatrix} \mathbf{L}_1^T\mathbf{L}_1 & \mathbf{L}_1^T\mathbf{L}_2 & \cdots & \mathbf{L}_1^T\mathbf{L}_p \\ \mathbf{L}_2^T\mathbf{L}_1 & \mathbf{L}_2^T\mathbf{L}_2 & \cdots & \mathbf{L}_2^T\mathbf{L}_p \\ \vdots & \vdots & \ddots & \vdots \\ \mathbf{L}_p^T\mathbf{L}_1 & \mathbf{L}_p^T\mathbf{L}_2 & \cdots & \mathbf{L}_p^T\mathbf{L}_p \end{pmatrix} = \begin{pmatrix} \mathbf{L}_1^T\mathbf{L}_1 & \mathbf{0} & \cdots & \mathbf{0} \\ \mathbf{0} & \mathbf{L}_2^T\mathbf{L}_2 & \cdots & \mathbf{0} \\ \vdots & \vdots & \ddots & \vdots \\ \mathbf{0} & \mathbf{0} & \cdots & \mathbf{L}_p^T\mathbf{L}_p \end{pmatrix} + \begin{pmatrix} \mathbf{0} & \mathbf{L}_1^T\mathbf{L}_2 & \cdots & \mathbf{L}_1^T\mathbf{L}_p \\ \mathbf{L}_2^T\mathbf{L}_1 & \mathbf{0} & \cdots & \mathbf{L}_2^T\mathbf{L}_p \\ \vdots & \vdots & \ddots & \vdots \\ \mathbf{L}_p^T\mathbf{L}_1 & \mathbf{L}_p^T\mathbf{L}_2 & \cdots & \mathbf{0} \end{pmatrix}. \quad (8)$$

Here, we divide the multiparameter Hessian into two terms. The first term is associated with the Hessian submatrices for the same parameter classes $\mathbf{L}_i^T\mathbf{L}_i$. The second term is associated with the Hessian submatrices for different parameter classes $\mathbf{L}_i^T\mathbf{L}_j$ $(i \neq j)$. According to equation 3, the first term yields a blurred version of the actual reflectivity model, while the second term explains the crosstalk artifacts introduced by the coupling effects in multiparameter migration image. Traditionally, the coupling effect is intuitively evaluated by displaying diffraction pattern (Tarantola, 1986; Virieux and Operto, 2009; Operto et al., 2013).

Decoupled deblurring filter algorithm

In the context of multiparameter seismic inversion, the crosstalk artifacts can also be reduced by an accurate estimate of the multiparameter Hessian inverse according to equation 5. In this article, we propose to estimate the multiparameter Hessian inverse based on a localized filter, denoted as the decoupled deblurring filter. The deblurring filter for a single parameter class (Aoki and Schuster, 2009) is based on the assumption that the Hessian is a diagonally dominant matrix. Our decoupled deblurring filter further assumes that the submatrices of the Hessian for different parameter classes $\mathbf{L}_i^T\mathbf{L}_j$ $(i \neq j)$ are also diagonally dominant.

According to equation 8, the multiparameter Hessian inverse $(\mathbf{L}^T\mathbf{L})^{-1}$ can also be written as a combination of $p \times p$ submatrices

$$(\mathbf{L}^T\mathbf{L})^{-1} = \mathbf{F} = \begin{pmatrix} \mathbf{F}_{1,1} & \mathbf{F}_{1,2} & \cdots & \mathbf{F}_{1,p} \\ \mathbf{F}_{2,1} & \mathbf{F}_{2,2} & \cdots & \mathbf{F}_{2,p} \\ \vdots & \vdots & \ddots & \vdots \\ \mathbf{F}_{p,1} & \mathbf{F}_{p,2} & \cdots & \mathbf{F}_{p,p} \end{pmatrix}, \quad (9)$$

where $(\mathbf{L}^T\mathbf{L})^{-1}$ is denoted as $\mathbf{F}$ and its submatrices $\mathbf{F}_{l,k}$ $(k, l = 1, 2, \ldots, p)$ have the same dimension. According to equation 5 and the notation in equation 7, we have

$$\sum_{k=1}^{p} \mathbf{F}_{l,k}\mathbf{m}_k^{\text{mig}} = \mathbf{m}_l, \forall l, \quad (10)$$

where $\forall l$ means equation 10 is a systerm of p equations $(l = 1, 2, \ldots, p)$. For the decoupled deblurring filter, we seek p^2 stationary local filters $\mathbf{f}_{k,l}$ to approximate the p^2 submatrices $\mathbf{F}_{l,k}$ in a window

$$\sum_{k=1}^{p} \mathbf{f}_{l,k} * [\mathbf{m}_k^{\text{mig}}] \approx [\mathbf{m}_l], \forall l \quad (11)$$

where [ ] denotes the model or migration image in a window.

The filter $\mathbf{f}_{l,k}$ can be computed by constraining them to a set of equations

$$\sum_k \mathbf{f}_{l,k} * [(\mathbf{m}_i^{\text{mig\_ref}})_k] = [(\mathbf{m}_i^{\text{ref}})_l], \ \forall i, l. \quad (12)$$

Here $i = 1, 2, ..., p$ is the index of the designed reference multiparameter model. Each $\mathbf{m}_i^{\text{ref}}$ is a model of p parameter classes and $\mathbf{m}_i^{\text{mig\_ref}}$ is the corresponding migration image with the form illustrated in equation 7:

$$\mathbf{m}_i^{\text{ref}} = \begin{pmatrix} (\mathbf{m}_i^{\text{ref}})_1 \\ (\mathbf{m}_i^{\text{ref}})_2 \\ \vdots \\ (\mathbf{m}_i^{\text{ref}})_p \end{pmatrix} \text{ and } \mathbf{m}_i^{\text{mig\_ref}} = \begin{pmatrix} (\mathbf{m}_i^{\text{mig\_ref}})_1 \\ (\mathbf{m}_i^{\text{mig\_ref}})_2 \\ \vdots \\ (\mathbf{m}_i^{\text{mig\_ref}})_p \end{pmatrix}. \quad (13)$$

There are p reference multiparameter models and their corresponding migration images are used to solve equation 12. This means that equation 12 is a set of p^2 equations and the solution is p^2 filters.

For simplicity, we design the $(\mathbf{m}_i^{\text{ref}})_i$ to represents a model with an even distribution of isolated point diffractors, and $(\mathbf{m}_i^{\text{ref}})_l = 0$ $(i \neq l)$ with no diffractors. An example of reference models with two parameter classes $(p = 2)$ is shown in Figure 1. The reference models are then divided into several subsections centered at the location of each point diffractor. For example, a subsection is displayed as the area of the black dashed squares in Figure 2. In each subsection, $\mathbf{f}_{l,k}$ is assumed to be stationary and is calculated according to equation 12. The size of $[(\mathbf{m}_i^{\text{mig\_ref}})_k]$ has to be big enough to cover the main part of the migration butterflies (Schuster and Hu, 2000) of each parameter class. Since all $\mathbf{f}_{l,k}$ are local filters, they approximate the near-diagonal terms of $\mathbf{F}_{l,k}$.

The size of the local filter $\mathbf{f}_{l,k}$ is small so equation 12 can be solved by the least-squares method. After calculating $\mathbf{f}_{l,k}$, we apply them to each subsection of the migration image $[\mathbf{m}_k^{\text{mig}}]$ to approximate the model in that subsection $[\mathbf{m}_l]$ according to equation 11. We can also rewrite equation 11 into matrix notation

$$\mathbf{m} \approx \mathbf{F}_a\mathbf{m}^{\text{mig}}. \quad (14)$$

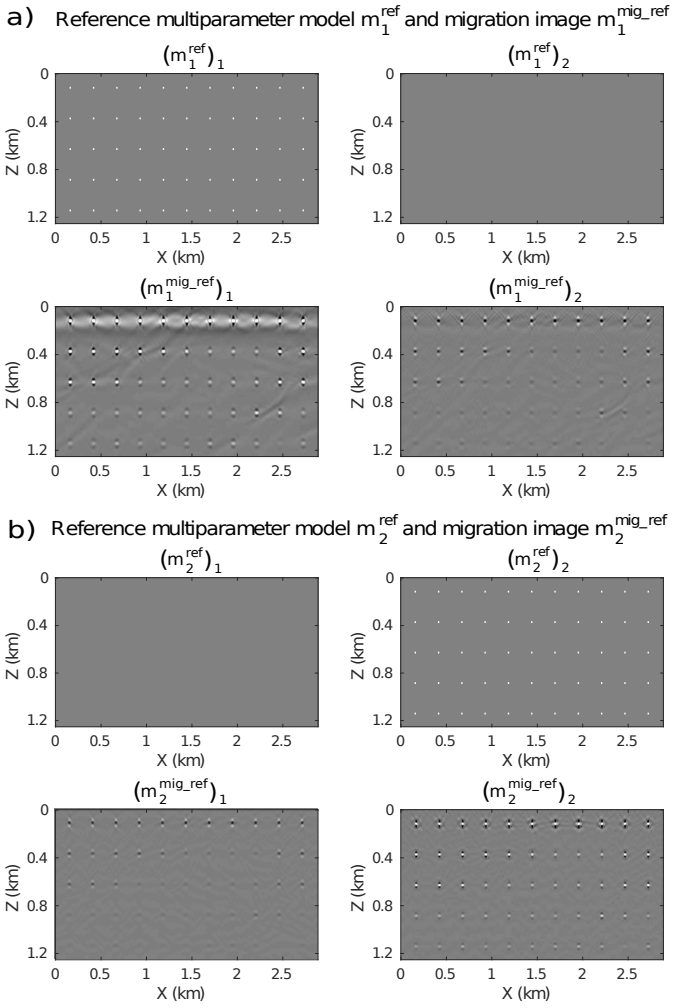

Figure 1: An example of reference reflectivity models of two parameter classes containing isolated point diffractors and their corresponding migration images. The point diffractors are indicated by the white dots in $(\mathbf{m}_1^{\text{ref}})_1$ and $(\mathbf{m}_2^{\text{ref}})_2$.

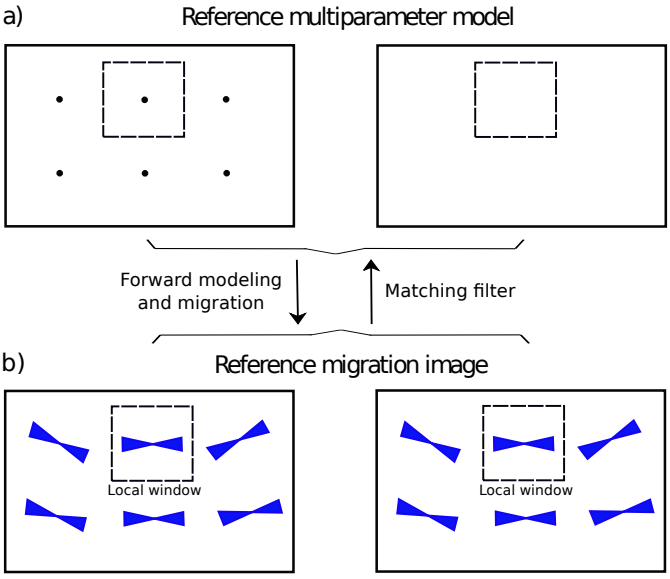

Figure 2: Illustration of local matching filters that transform the migration image ($\mathbf{m}_1^{\text{mig\_ref}}$) to its reference model ($\mathbf{m}_1^{\text{ref}}$) for two parameter classes ($p = 2$). The four black squares belong to the same subsection. The two red dashed squares represent four local filters in this subsection. Note that the local filters is constant within the subsection.

This means that the computed $\mathbf{F}_a$ can be used as the approximate Hessian inverse:

$$\mathbf{F}_a \approx \mathbf{F}, \text{where } \mathbf{F} = (\mathbf{L}^T\mathbf{L})^{-1}. \tag{15}$$

We can improve the accuracy of the multiparameter migration image by applying $\mathbf{F}_a$ to it, or we can use $\mathbf{F}_a$ as a preconditioner in an iterative multiparameter inversion to speed up the convergence (Dai et al., 2011).

Note that there is a flexibility for designing p reference models $\mathbf{m}_i^{\text{ref}}$ as input for equation 12. For example, we can also place a point diffractor at the center of $[(\mathbf{m}_i^{\text{ref}})_l]$ $(i \neq l)$, as long as $[\mathbf{m}_1^{\text{ref}}], [\mathbf{m}_2^{\text{ref}}], \cdots, [\mathbf{m}_p^{\text{ref}}]$ are linearly independent in every subsection.

NUMERICAL RESULTS

We now demonstrate with synthetic elastic data that the proposed decoupled deblurring filter can reduce artifacts in elastic migration and inversion images.. The synthetic data are simulated from two land models: (1) a layered model with different P- and S-wave velocity anomalies and 2) a portion of the modified Marmousi2 model.

In the synthetic examples, the observed two-component data are generated by a time-space staggered-grid solution of the elastic wave equation (Levander, 1988) without a free-surface condition. The data are used to inverted for the reflectivity model of the P- and S-wave velocities $\mathbf{m} = (\delta V_p/V_p, \delta V_s/V_s)^T$ using elastic reverse time migration (RTM) and least-squares reverse time migration (LSRTM) (Feng and Schuster, 2016), where V_p and

V_s are the background P- and S-wave velocity models and δV_p and δV_s are the corresponding perturbations.

The diffraction pattern of the reflectivity model for incident P-waves is shown in Figure 3. Here, the reflectivity images of the P- and S-wave velocities are denoted as the P-image and the S-image, respectively. Elastic RTM refers to the first iteration of elastic LSRTM. If a decoupled deblurring filter is not used, source-side illumination (Plessix and Mulder, 2004) is used as the preconditioning factor for elastic LSRTM, and the elastic RTM results are illumination compensated.

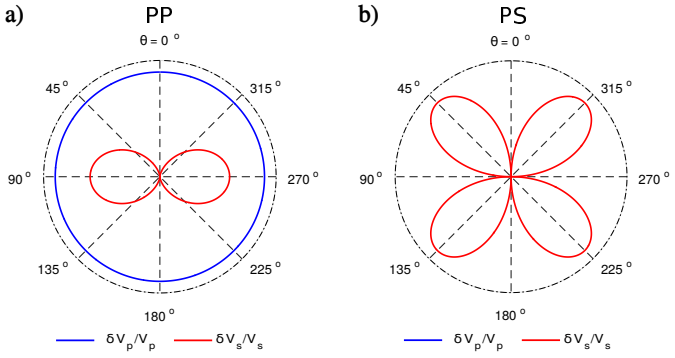

Figure 3: Diffraction radiation patterns of the P- and S-reflectivity models for two scattering modes, (a) PP and (b) PS. The scattering radiation patterns are plotted as polar coordinates as a function of the scattering (or aperture) angle. Note that the P-wave impedance perturbation generates only PP diffraction with an isotropic diffraction pattern (Vincent et al., 2013b).

Layered velocity model

We first demonstrate that a decoupled deblurring filter can improve the quality of the elastic migration image, where the input data are generated for the flat-layered elastic model embedded with anomalies in Figure 4. The density is homogeneous with 1 g/cm^3. Here 92 shots are evenly spaced at 50 m, and 230 receivers are evenly distributed at 20 m intervals on the surface. The P-wave point source uses a Ricker wavelet with a 7.5 Hz peak frequency and the total recording time is 5 s.

Figure 5 compares the elastic RTM images with and without the decoupled deblurring filter. The images with filtering have fewer artifacts, better amplitude balancing and higher resolutions compared to the images without filtering. In addition, the P- and S-images without filtering contain false reflectivity images of P- and S-wave velocity anomalies. Note that the crosstalk also exists at the flat layered interfaces in the images, but it overlaps with the true images. The crosstalk problem is mitigated after applying the decoupled deblurring filter.

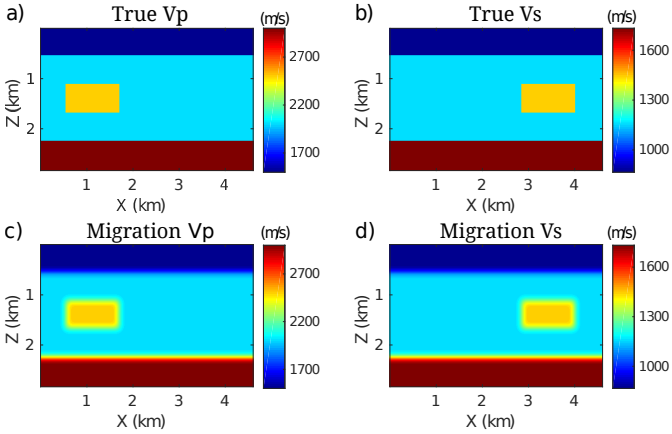

Figure 4: Layered model: (a) true V_p, (b) true V_s models. The migration velocity models for V_p and V_s are shown in c) and d), respectively.

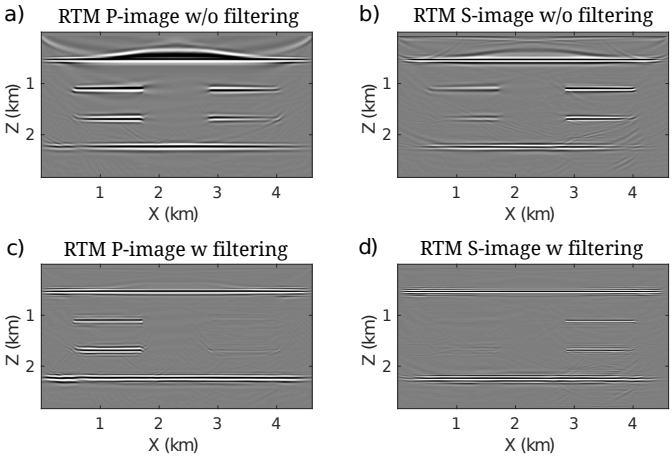

Figure 5: Migration images from elastic RTM without decoupled deblurrring filter for (a) P image and (b) S image, elastic RTM with decoupled deblurrring filter for (c) P image and (d) S image.

Marmousi2 velocity model

We also demonstrate that the the decoupled deblurring filter can be used as a preconditioner to improve the quality of images and speed up the convergence for elastic LSRTM. We use a portion of the elastic Marmousi2 model and replace the water layer with a solid layer. The S-wave velocity is also modified to avoid very low V_s values. Figures 6a and 6c show the true P- and S-wave velocity models, respectively. The velocity models for migration are shown in Figures 6b and 6d, where the density is constant at 1 g/cm^3. The true reflectivity models for P- and S-wave velocities are shown in Figure 7, which only used for comparison with the migration images. 393 shots are evenly spaced at 20 m, and 787 receivers are evenly distributed at 10 m intervals on the surface. The P-wave point source uses a Ricker wavelet with a 15-Hz peak frequency and the total recording time is 5.5 s.

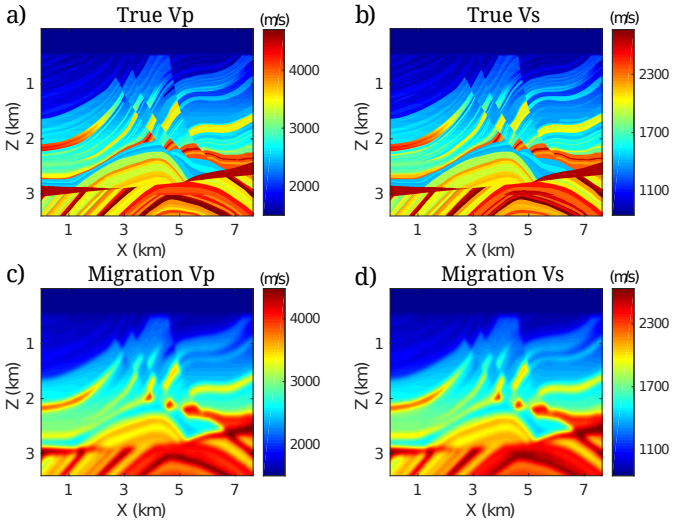

Figure 6: A portion of the modified Marmousi2 model: (a) true V_p, (b) migration V_p, (c) true V_s, and (d) migration V_s.

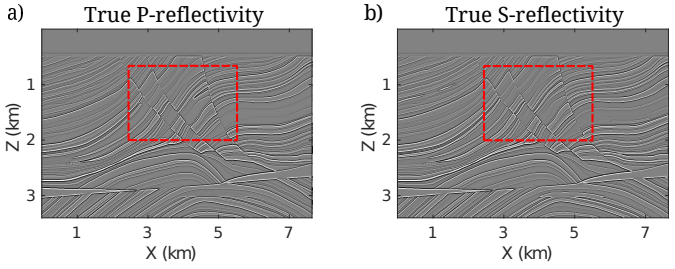

Figure 7: The Marmousi2 reflectivity models: true reflectivity model for (a) P-wave velocity and (b) S-wave velocity.

The elastic RTM images with and without the decoupled deblurring filter are shown in Figure 8. The elastic LSRTM images with and without the decoupled deblurring filter as a preconditioner are shown in Figure 9. The deblurring filter improves the quality of both the RTM and LSRTM images . The filter also expedites the convergence so that the misfit function of the filtered LSRTM at the 6th iteration is about the same as the one without the filter at the 15th iteration, as shown in Figure 10.

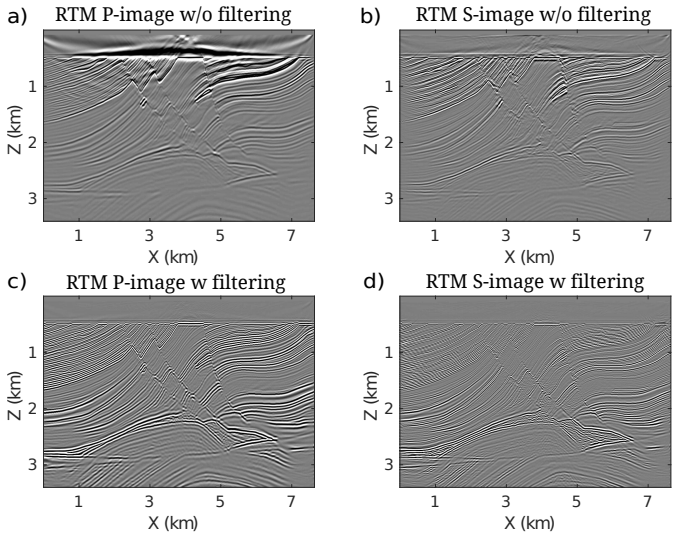

Figure 8: Elastic RTM images of the Marmousi2 model: without decoupled deblurrring filter for (a) P-image and (b) S-image, with decoupled deblurrring filter for (c) P-image and (d) S-image.

The zoom views of the red-box area (indicated in Figure 7) for the P-images (Figure 11) and S-images (Figure 12) also show that the decoupled deblurring filter improves the amplitude balance and resolution of the images. The filtered LSRTM image has the best resolution compared to other images, as illustrated in the wavenumber spectra in Figures 11b and 12b. In the yellow box of Figure 11f, the two reflectors are only distinguishable in the filtered LSRTM P-image. In addition, the RTM S-image without filtering (Figure 12c) shows a strong false structure in the reservoir area, for example, the green box indicated in Figure 11a and 12a. These crosstalk artifacts are much weaker in either the LSRTM S-image without filtering (Figure 12d) or the RTM S-image with filtering (Figure 12e). This crosstalk problem is slightly mitigated by LSRTM with filtering, as shown in Figure 12f. All the P-images show a consistent structure in this reservoir area.

DISCUSSION

Approximating the matrix for the multiparameter Hessian inverse is an ill-posed problem (Virieux and Operto, 2009; Vincent et al., 2013a; Operto et al., 2013). Therefore, the calculated deblurring filter might amplify the noise in the images even though the resolution is improved and the crosstalk artifact is reduced. This problem can be mitigated by using a strong regularization for solving equation 12, yet too much regularization can reduce resolution and amplify crosstalk noise. These problems can be

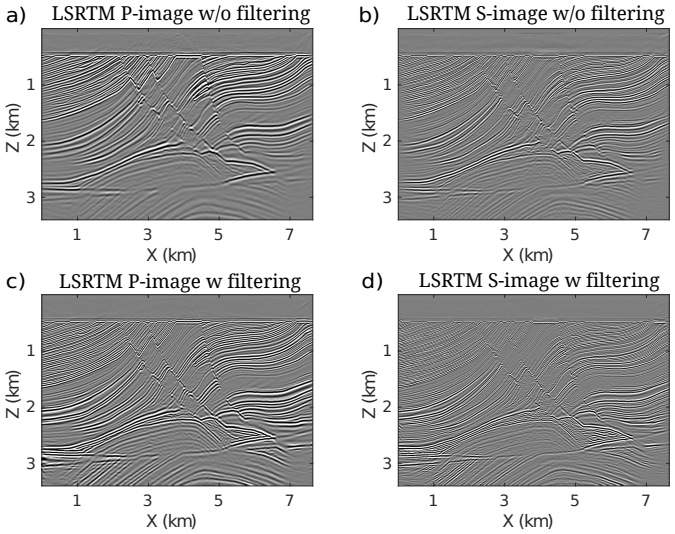

Figure 9: Elastic LSRTM images of the Marmousi2 model: without decoupled deblurrring filter as preconditioning for (a) P-image and (b) S-image, with decoupled deblurrring filter as preconditioning for (c) P-image and (d) S-image.

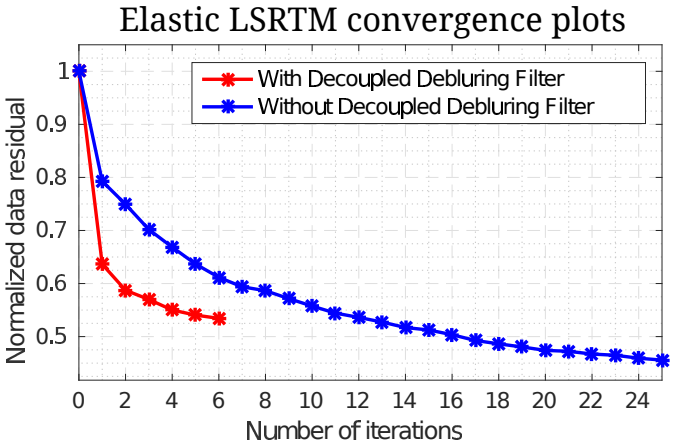

Figure 10: Convergence curves for elastic LSRTM with and without filtering for Marmousi2 model.

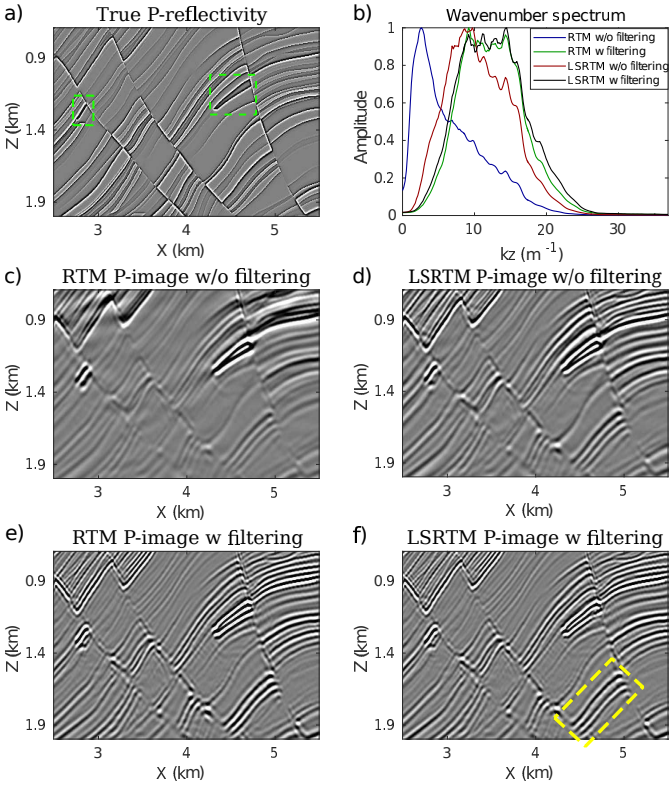

Figure 11: Zoom views showing the P-images in the red boxes in Figure 8 and 9. (a) True P-reflectivity image used only for comparison, (b) average z-direction wavenumber spectra for the P-images in the zoom view area, (c) RTM and (d) LSRTM P-images without filter, (e) RTM and (f) LSRTM P-images with filter.

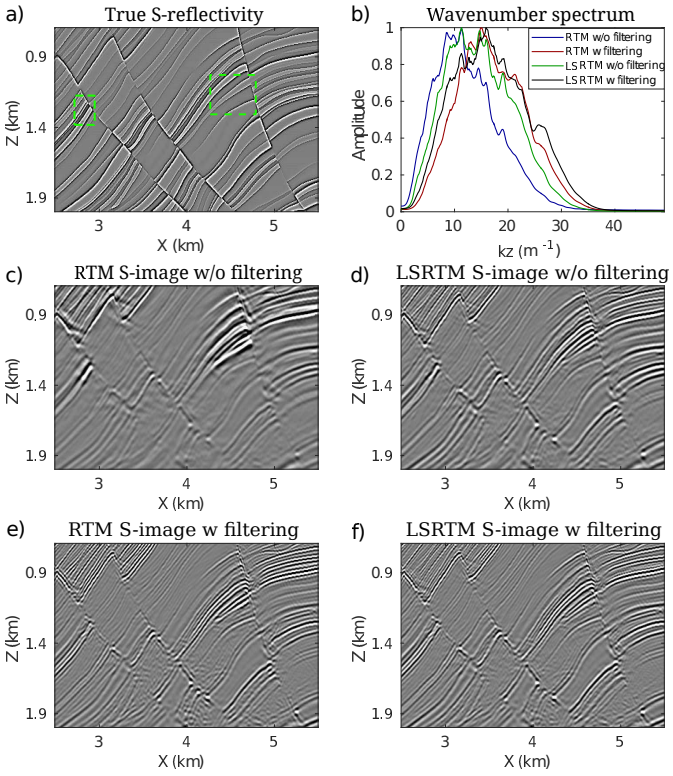

Figure 12: Zoom views showing the S-images in the red boxes in Figure 8 and 9. (a) True S-reflectivity image used only for comparison, (b) average z-direction wavenumber spectra for the S-images in the zoom view area, (c) RTM and (d) LSRTM S-images without filter, (e) RTM and (f) LSRTM S-images with filter.

relieved by increasing the number of least-squares iterations.

The proposed decoupled deblurring filter can also be applied to elastic full waveform inversion (FWI) (Tarantola, 1986; Mora, 1987; Sears et al., 2010), where the deblurring filter needs to be updated every few iterations. It can also be applied to the inversion of other parameter classes.

CONCLUSION

We present an approximation to the mutiparameter Hessian inverse using local filters to approximate the submatrices of the Hessian inverse. The calculation of the filters requires matching a series of simulated multiparameter images to their reference models. Numerical tests on the elastic migration and inversion for the reflectivity images of P- and S-wave velocities show that the decoupled debluring filter not only reduces the footprint noise, balances the amplitude and increases the resolution of the multiparameter migration images, but also mitigates the crosstalk artifacts. When used as a preconditioner, it also significantly accelerates the convergence speed in the multiparameter inversion. The computational cost for the calculation of these deblurring filters is about p migration.

ACKNOWLEDGEMENTS

The research is supported by the King Abdullah University of Science and Technology (KAUST) in Thuwal, Saudi Arabia. We are grateful to the sponsors of the Center for Subsurface Imaging and Modeling (CSIM) Consortium for their financial support. The first author would also like to thank Bowen Guo for his help. The computation resource provided by the KAUST Supercomputing Laboratory (KSL) is greatly appreciated.

APPENDIX A

ADJOINT EQUATION AND GRADIENTS FOR ELASTIC LEAST-SQUARES REVERSE TIME MIGRATION

REFERENCES

Aoki, N. and G. T. Schuster, 2009, Fast least-squares migration with a deblurring filter: Geophysics, **74**, WCA83–WCA93.

Claerbout, J. F., 1992, Earth soundings analysis: processing versus inversion: Blackwell Scientific Publications.

Dai, W., X. Wang, and G. T. Schuster, 2011, Least-squares migration of multisource data with a deblurring filter: Geophysics, **76**, R135–R146.

Duan, Y., P. Sava, and A. Guitton, 2016, Elastic least-squares reverse time migration: 76th Annual International Meeting, Expanded Abstracts, 4152–4157, SEG.

Duquet, B., K. J. Marfurt, and J. A. Dellinger, 2000, Kirchhoff modeling, inversion for reflectivity, and subsurface illumination: Geophysics, **65**, 1195–1209.

Feng, Z. and G. Schuster, 2016, Elastic least-squares reverse time migration, 4163–4167. SEG.

Guitton, A., 2004, Amplitude and kinematic corrections of migrated images for nonunitary imaging operators: Geophysics, **69**, 1017–1024.

Hu, J., G. T. Schuster, and P. A. Valasek, 2001, Poststack migration deconvolution: Geophysics, **66**, 939–952.

Lailly, P., 1983, The seismic inverse problem as a sequence of before stack migrations: Conference on Inverse Scattering, Expanded Abstracts, 206–220, Theory and Application.

———, 1984, Migration methods: partial but efficient solutions to the seismic inverse problem: Inverse Problems of Acoustic and Elastic Waves, **51**, 13871403.

Levander, A. R., 1988, Fourth-order finite-difference P-SV seismograms: Geophysics, **53**, 1425–1436.

Mora, P., 1987, Nonlinear two-dimensional elastic inversion of multioffset seismic data: Geophysics, **56**, 1211–1228.

Nemeth, T., C. Wu, and G. T. Schuster, 1999, Least-squares migration of incomplete reflection data: Geophysics, **64**, 208–221.

Operto, S., Y. Gholami, R. Brossier, L. Métivier, V. Prieux, A. Ribodetti, and J. Virieux, 2013, A guided tour of multi-parameter full waveform inversion with multi-component data: from theory to practice: The Leading Edge, **32**, 1040–1054.

Plessix, R. and W. Mulder, 2004, Frequency-domain finite-difference amplitude-preserving migration: Geophysical Journal International, **157**, 975–987.

Pratt, R. G., C. Shin, and G. J. Hicks, 1988, Two-dimensional non-linear inversion of seismic waveforms: numerical results: Geophysical Journal International, **133**, 341–362.

Rickett, J. E., 2003, Illuminationbased normalization for waveequation depth migration: GEOPHYSICS, **68**, 1371–1379.

Schuster, G. T. and J. Hu, 2000, Greens function for migration: Continuous recording geometry: Geophysics, **65**, 167–175.

Sears, T. J., P. J. Barton, and S. C. Singh, 2010, Elastic full waveform inversion of multicomponent ocean-bottom cable seismic data: Application to alba field, u. k. north sea: Geophysics, **75**, R109–R119.

Symes, W. W., 2008, Approximate linearized inversion by optimal scaling of prestack depth migration: GEOPHYSICS, **73**, R23–R35.

Tang, Y., 2009, Target-oriented wave-equation least-squares migration/inversion with phase-encoded hessian: Geophysics, **74**, WCA95–WCA107.

Tang, Y. and S. Lee, 2015, Multi-parameter full wavefield inversion using non-stationary point-spread functions: 75th Annual International Meeting, Expanded Abstracts, 1111–1115, SEG.

Tarantola, A., 1984, Inversion of seismic reflection data in the acoustic approximation: Geophysics, **49**, 1259–1266.

———, 1986, A strategy for nonlinear elastic inversion of seismic reflection data: Geophysics, **51**, 1893–1903.

Vincent, P., B. Romain, S. Operto, and V. Jean, 2013a, Multiparameter full waveform inversion of multicomponent ocean-bottom-cable data from the valhall field. part 1: imaging compressional wave speed, density and attenuation: Geophysical Journal International.

———, 2013b, Multiparameter full waveform inversion of multicomponent ocean-bottom-cable data from the valhall field. part 2: imaging compressive-wave and shear-wave velocities: Geophysical Journal International, **194**, 1665–1681.

Virieux, J. and S. Operto, 2009, An overview of full-waveform inversion in exploration geophysics: Geophysics, **74**, WCC1–WCC26.

Wang, Y., L. Dong, Y. Liu, and J. Yang, 2016, 2d frequency-domain elastic full-waveform inversion using the block-diagonal pseudo-hessian approximation: GEOPHYSICS, **81**, R247–R259.

Wang, Y. and R. G. Pratt, 1997, Sensitivities of seismic traveltimes and amplitudes in reflection tomography: Geophysical Journal International, **131**, 618–642.

Yu, J., J. Hu, G. T. Schuster, and R. Estill, 2006, Prestack migration deconvolution: Geophysics, **71**, S53–S62.